A&A 677, A188 (2023)
https://doi.org/10.1051/0004-6361/202346912

Astronomy & Astrophysics

Central radio galaxies in galaxy clusters: Joint surveys by eROSITA and ASKAP

K. Böckmann[1], M. Brüggen[1], B. Koribalski[2,3], A. Veronica[4], T. H. Reiprich[4], E. Bulbul[5], Y. E. Bahar[5], F. Balzer[5], J. Comparat[5], C. Garrel[5], V. Ghirardini[5], G. Gürkan[6,7,8], M. Kluge[5], D. Leahy[9], A. Merloni[5], A. Liu[5], M. E. Ramos-Ceja[5], M. Salvato[5], J. Sanders[5], S. Shabala[10], and X. Zhang[5]

[1] Hamburger Sternwarte, Universität Hamburg, Gojenbergsweg 112, 21029 Hamburg, Germany
e-mail: kathrin.boeckmann@hs.uni-hamburg.de
[2] Australia Telescope National Facility, CSIRO Astronomy and Space Science, PO Box 76, Epping, NSW 1710, Australia
[3] School of Science, Western Sydney University, Locked Bag 1797, Penrith, NSW 2751, Australia
[4] Argelander Institute for Astronomy (AIfA), University of Bonn, Auf dem Hügel 71, 53121 Bonn, Germany
[5] Max-Planck-Institut für extraterrestrische Physik, Gießenbachstraße 1, 85748 Garching, Germany
[6] Center for Astrophysics Research, Department of Physics, Astronomy and Mathematics, University of Hertfordshire, College Lane, Hatfield AL10 9AB, UK
[7] Thüringer Landessternwarte, Sternwarte 5, 07778 Tautenburg, Germany
[8] CSIRO Space and Astronomy, ATNF, PO Box 1130, Bentley, WA 6102, Australia
[9] Department of Physics and Astronomy, University of Calgary, Calgary, Alberta T2N 1N4, Canada
[10] School of Natural Sciences, University of Tasmania, Private Bag 37, Hobart, Tasmania 7001, Australia

Received 16 May 2023 / Accepted 25 July 2023

ABSTRACT

Contact. The extended ROentgen Survey with an Imaging Telescope Array (eROSITA) telescope on board the Spectrum-Roentgen-Gamma (SRG) mission has completed the first eROSITA All-Sky Survey (eRASS:1). It detected ∼10^4 galaxy clusters in the western Galactic hemisphere. In the radio band, the Australian Square Kilometre Array Pathfinder (ASKAP) telescope completed its pilot 1 phase of the project Evolutionary Map of the Universe (EMU) with 220 000 sources in a 270 deg^2 field overlapping with eRASS:1. These two surveys are used to study radio-mode active galactic nuclei in clusters.
Aims. In order to understand the efficiency of radio-mode feedback at the centers of galaxy clusters, we relate the radio properties of the brightest cluster galaxies to the X-ray properties of the host clusters.
Methods. We identified the central radio sources in eRASS:1 clusters or calculated corresponding upper limits on the radio luminosity. Then, we derived relations between the X-ray properties of the clusters and the radio properties of the corresponding central radio source.
Results. In total, we investigated a sample of 75 clusters. We find a statistically significant correlation between the X-ray luminosity of the cluster and the 944 MHz radio luminosity of the corresponding central radio galaxy. There is also a positive trend between the radio power and the largest linear size of the radio source. The density and the largest linear size are not correlated. We find that the kinetic luminosity of the radio jets in high-luminosity clusters with $L_X > 10^{43}$ erg s^{-1} is no longer correlated with the X-ray luminosity, and we discuss various reasons. We find an anticorrelation between the central cooling time t_{cool} and the radio luminosity L_R, indicating a need for more powerful active galactic nuclei in clusters with short central cooling times.

Key words. X-rays: galaxies: clusters – radio continuum: galaxies – galaxies: clusters: intracluster medium – galaxies: active – galaxies: clusters: general

1. Introduction

The hot gas in galaxy clusters, called the intracluster medium (ICM), is strongly affected by feedback of active galactic nuclei (AGN). AGN reside in the dominant cD galaxies of clusters, which host the most massive black holes of the Universe. Two different modes of AGN feedback are found in observations: the radiative or quasar mode, and the radio or jet mode (Cattaneo et al. 2009; Heckman & Best 2014). The radiative mode causes uniform heating of the environment around it, whereas in radio mode, AGN jets expel radio-heated gas from the accreting black hole matter into the ICM and push the existing X-ray heated cluster gas away (Shabala et al. 2020). Therefore, on the one hand, AGN activity prevents the cooling of gas and subsequent star formation, and on the other hand, AGN contribute to star formation by projecting jets toward the ICM and compressing the gas. An increment of radiative losses of the ICM in turn leads to an increment in heating of the gas by the AGN. The more gas cools, the higher the energy output that is able to quench the radiative losses. This is known as the AGN feedback loop (McNamara et al. 2016; Gaspari et al. 2020). AGN feedback has been observed in a wide range of systems, from isolated elliptical galaxies to massive clusters. The most powerful AGN operating in radio mode can be found in the brightest cluster galaxies (BCGs), which usually are massive elliptical galaxies residing at the bottom of the clusters potential (e.g., reviews by Fabian 2012; Gitti et al. 2012; McNamara & Nulsen 2012).

Ineson et al. (2013, 2015) performed a study of the interplay between AGN and their environment in a sample of radio-loud AGN galaxy clusters and galaxy groups. As a result, they found

a correlation between the X-ray emission from the ICM and the power of the corresponding central radio source at 151 MHz. They argued that this correlation could arise from AGN in a phase of radiatively inefficient accretion, which are also called low-excitation radio galaxies (LERGs), while high-excitation radio galaxies (HERGs) stand out of the distribution and show higher radio powers. However, it is important to note that the origin of this relation is not obvious as X-ray emission in clusters and groups is mostly due to line emission and Bremsstrahlung that allows the ICM to cool. Therefore, the timescale of these radiative losses is strongly dependent on the distance of the diffuse gas from the cluster core, which varies from less than 1 Gyr in the center of the strongest cool-cores to a few billion years in the outskirts. Nipoti & Binney (2005), on the other hand, suggested that the AGN power output reoccurs and acts in cycles of $\sim 10^8$ yr. As a consequence, the timescales of these two processes are usually significantly different. On the other hand, Hardcastle et al. (2019) suggested that the majority of sources are compact and therefore short-lived, and so the cycle is many short-lived ($\sim$1 Myr) intermittent bursts (see also Shabala et al. 2008). Pasini et al. (2020, 2021, 2022) investigated the radio power of the central radio galaxy in galaxy clusters and in galaxy groups at different wavelengths. The authors also found positive correlations between the radio power of the central AGN at frequencies from 144 MHz to 1.4 GHz and the main properties of the diffuse X-ray intragroup and intracluster medium, again suggesting a link between AGN heating and cooling processes in the gaseous halo (Pope et al. 2012).

Deep X-ray observations with *XMM-Newton* and *Chandra* have revealed that most of the systems with radio-mode AGN have disturbed X-ray morphologies caused by AGN-ejected jets. These surface brightness features, including cavities in the X-ray images and sharp density discontinuities that are interpreted as shocks, indicate a strong correlation between the ICM and the central AGN. The thermodynamical properties of the intracluster gas is also affected by AGN feedback in teRMS of the gas entropy distribution and transport of high-metallicity gas from the center of the cluster to its outskirts. The X-ray cavities or bubbles that have been discovered in X-ray images of clusters are often filled with radio emission. This leads to the assumption that radio plasma produced by AGN outflows displaces the X-ray emitting gas of the ICM. One of the main results of these observations was the revelation of a scaling relation between the cavity power and the radio luminosity (Bîrzan et al. 2004, 2020; Rafferty et al. 2006; Timmerman et al. 2022).

The extended ROentgen Survey with an Imaging Telescope Array (eROSITA) on board the Spectrum-Roentgen-Gamma (SRG) mission was launched in July 2019 (Predehl et al. 2021). eROSITA will perform all-sky surveys (eRASS) with a significantly improved sensitivity compared to the ROSAT all-sky survey. In contrast to X-ray telescopes such as *XMM-Newton* or *Chandra*, which are used for long-exposure pointed observations of single targets, eROSITA allows unique survey science capabilities by scanning large areas of the X-ray sky fast and efficiently. The eRASS survey is detecting a large number of previously undetected galaxy clusters and will substantially extend existing galaxy cluster catalogs (Merloni et al. 2012; Liu et al. 2022).

In this work, we make use of the cluster catalog resulting from the first all-sky scan (eRASS:1), which was completed in 2020 (Bulbul et al., in prep.). We study the central radio galaxies in the cluster centers with 944 MHz radio data from the survey called Evolutionary Map of the Universe (EMU) that was performed by the Australian Square Kilometre Array Pathfinder (ASKAP; Norris et al. 2021).

The paper is structured as follows: in Sect. 2 we explain how our sample was created, and we display its main properties. In Sect. 3 we examine and discuss the correlation between the radio and the X-ray emission from our sample in comparison to other correlations. Finally, we conclude in Sect. 4. Throughout this paper, we assume the standard ΛCDM cosmology with $H_0 = 70\,\mathrm{km\,s^{-1}\,Mpc^{-1}}$, $\Omega_\Lambda = 0.7$, and $\Omega_\mathrm{M} = 0.3$.

2. Data

2.1. eRASS:1 cluster catalog

eROSITA is an X-ray space telescope operating in the 0.2–10 keV energy range on board the SRG mission (Sunyaev et al. 2021; for more information on this mission, see, e.g., the instrument paper by Predehl et al. 2021). It has an effective area of 1365 $\mathrm{cm^2}$ and a spectral resolution of 80 eV FWHM (Full Width at Half Maximum) at 1 keV and an angular survey resolution of 26 arcsec. The first task of eROSITA is to scan the whole X-ray sky with a final depth of about 1.3 ks. The sensitivity will therefore be improved by at least a factor of 20 compared to the only previous X-ray all-sky survey performed by ROSAT 30 years ago. The main task of eROSITA is the study of evolution and nature of dark energy. eROSITA is expected to detect about 10^5 galaxy clusters and more than one million AGN (Merloni et al. 2012, 2020).

The first all-sky survey eRASS:1 imaged the whole X-ray sky over the course of 182 days from December 2019 to June 2020, with an average effective exposure of 150–200 s. About 10^4 clusters are detected as extended sources in eRASS:1 using the source detection algorithm in the eROSITA Standard Analysis Software System (eSASS; Brunner et al. 2022). Redshifts are determined using data from the Legacy Survey. Details about the eRASS:1 galaxy cluster catalog can be found in Bulbul et al. (in prep.). The X-ray luminosity that is used throughout this paper was calculated in the 0.2–2.3 keV band.

2.2. EMU pilot field

The Australian Square Kilometer Array Pathfinder (ASKAP) is a radio telescope in the Murchison region of Western Australia (Johnston et al. 2008; Hotan et al. 2021; Koribalski 2022). ASKAP is a radio interferometer consisting of 36 12-meter dish antennas, spread out in two dimensions with baselines up to 6 km. Each antenna is equipped with a wide-field phased array feed (PAF) that is used to form 36 beams, that is, each pointing reaches a field of view of $\sim 30\,\mathrm{deg^2}$.

The survey project called evolutionary map of the Universe (EMU) uses the ASKAP telescope. In July to August 2019, EMU observed a pilot field for 100 h to test the planned observing mode for the full EMU survey. The EMU pilot survey mapped 270 $\mathrm{deg^2}$ of sky with a RA from 305° to 335° and Dec from −62° to −48°, centered at 944 MHz down to an RMS of about 25–30 $\mu\mathrm{Jy\,beam^{-1}}$ at an angular resolution of 10–18 arcsec (see Norris et al. 2011, 2021 for further details on the survey).

As images with large fields of view such as the EMU pilot field yield a large number of detected astronomical sources, an automated source detection technique that measures the properties of the sources is essential. The most common approach is to identify local peaks of emission above some threshold, and fitting two-dimensional Gaussians. As radio surveys have become deeper and wider in recent years, the number of sources in catalogs has grown enormously, such that manual source-finding

and identification is no longer feasible. An ASKAP/EMU source-finding challenge by Hopkins et al. (2015) that was carried out before the start of EMU tested several approaches for an automatic source detection. Source-finding and cataloging is the last step in the ASKAP data-processing pipeline (ASKAPsoft; e.g., Guzman et al. 2019; Wieringa et al. 2020) for all surveys such as continuum, HI emission and absorption, and polarization, carried out using Selavy (Whiting et al. 2017). More powerful source finders will likely be applied by each team to their specific projects.

The image data were first processed by the ASKAPsoft pipeline, and the subsequent source extraction of the final calibrated image used the software tool Selavy. This tool identifies radio islands with emissions higher than five times the local RMS, and it fits Gaussians to peaks of emission within the islands. The peak as well as the integrated radio flux of each island is computed and stored in a FITS catalog containing a total number of ∼220 000 radio islands, ∼180 000 of which are single-component sources. In comparison with previous surveys, EMU explores a novel region of parameter space because of the ASKAP wide field of view combined with high angular resolution as well good sensitivity. For a summary of the EMU pilot survey specifications, see Table 1.

2.3. Construction of the sample

The EMU pilot field is fully covered by eRASS:1. Therefore, we created a cluster sample with all eRASS:1 detected clusters within the EMU field, resulting in a total number of 75 confirmed eRASS:1 clusters. Each cluster was visually inspected in the EMU image as well as in WISE and in legacy optical data to identify the BCG of each cluster and the corresponding radio source to the BCG.

We identified the BCG and the corresponding central radio island for each cluster. For 64 of the 75 clusters, we found a central radio source within a distance of $\sim\theta$ to the BCG, where $\theta = 18$ arcsec, which is the synthesized beam of the radio observation. For the remaining 11 clusters, we set an upper limit of 3σ, where σ is the RMS noise of the EMU image of RMS = 35 µJy. Magliocchetti & Brüggen (2007) examined radio emission of 550 X-ray selected clusters and reported that only 27% host a central radio source. However, the difference in these results can be attributed to the depth of the respective datasets because the depth of the survey they used reaches only 3 mJy, whereas the EMU has a depth of 35 µJy.

Visual inspection of each source is the most reliable way to minimize the number of false identifications because at all separations, some radio identifications selected by the position offset alone will be random coincidences (Condon et al. 2002; Sadler et al. 2002; Mauch & Sadler 2007). Nonetheless, we still expect a fraction of false associations, which we describe via the P-statistics. This quantifies the probability that a radio source has a chance coincidence within a distance θ from a certain point, here our BCG candidate. It is given by

$$P(\theta) = 1 - e^{n\pi^2}, \tag{1}$$

with n denoting the number density of radio sources (Scott et al. 2008). When we assume a uniform distribution of radio sources of $n = 815\,\mathrm{deg}^{-2}$, which is the average source density from an ASKAP observation, we obtain $P(18\,\mathrm{arcsec}) = 6.6\%$ contamination. For the 64 clusters with a radio match, we therefore expect about three false associations.

Table 1. EMU pilot survey specifications.

Area of survey	270 deg^2
Synthesised beamwidth	13 arcsec × 11 arcsec *FWHM*
Frequency range	800–1088 MHz
RMS sensitivity	25–35 µJy beam^{-1}
Total integration time	10 × 10 h
Number of sources	∼200 000

2.4. Properties of the sample

The upper panel of Fig. 1 shows a histogram of the redshift distribution of our cluster sample. The majority of the clusters lie within a redshift range of $0.1 < z < 0.7$. Two outliers lie above $z > 0.8$. We used the best available redshift provided from the eRASS:1 cluster catalog, which can be spectroscopic or photometric redshifts. The lower panel of Fig. 1 shows the mass distribution. The mass was estimated via the $L_X - M_{500}$ correlation by Chiu et al. (2022). The masses of most of the clusters lie within $1\text{–}12 \times 10^{14}\,M_\odot$.

The luminosity of all radio sources was calculated including the following k-correction:

$$L_{\mathrm{Radio}} = 4\pi D_L^2 S_{\mathrm{Radio}} (1+z)^{\alpha-1}. \tag{2}$$

D_L is the luminosity distance at redshift z, and α is the spectral index, assumed to be 0.6. Figure 2 shows the radio luminosity distribution at 944 MHz versus the redshift of the sample. We also plot the theoretical flux cut in Fig. 2.

Next, we calculated the largest linear size (LLS) for each radio source. The LLS is defined as the linear size of the major axis of a source, and it is displayed in Fig. 3. The LLS is calculated within a 3σ isophote. When the radio source was not resolved, which was the case for six clusters, we treated the source as an upper limit with an LLS corresponding to the beam size. The LLS varied from ∼50 to ∼250 kpc. We also show the offset from each BCG to the X-ray center of the corresponding cluster. The majority of BCGs are found within 200 kpc around the X-ray peak of the cluster.

In Fig. 4 we show the radio and X-ray luminosity distribution functions of the cluster sample at 944 MHz and 0.5–2.0 keV. The overall radio luminosities lie within a range of $\sim 10^{29}$ and $\sim 10^{33}$ erg s^{-1} Hz^{-1}. The X-ray luminosities exhibit values from $\sim 10^{43}$ to $\sim 10^{45}$ erg s^{-1}.

2.5. WISE colors

One approach to identify AGN is a mid-infrared color criterion that is deduced from the separation between the power-law AGN spectrum and the blackbody stellar spectrum of galaxies, which has its peak at a rest-frame of 1.6 µm (Assef et al. 2010). We applied this technique to our sample by using the Wide-field Infrared Survey Explorer (WISE) survey, which mapped the whole sky in four different bands: 3.4, 4.6, 12, and 22 µm, referred to as $W1, W2, W3$, and $W4$, respectively (Wright et al. 2010). The color criterion we used is the difference of the magnitudes of $W1-W2$ (i.e., 3.4–4.6). For our sample, the $W1$ and $W2$ magnitudes and the $W1-W2$ criterion are shown in Fig. 5. Our median value for the color criterion is $\mu \approx 0.152$, with a corresponding interquartile range of $\sigma \approx 0.155$. This is in contrast to Stern et al. (2012), who reported a value of $W1-W2 \geq 0.8$ for their AGN selection, and Assef et al. (2018), who reported a value of $W1-W2 \geq 0.77$. However, LaMassa et al. (2019) and

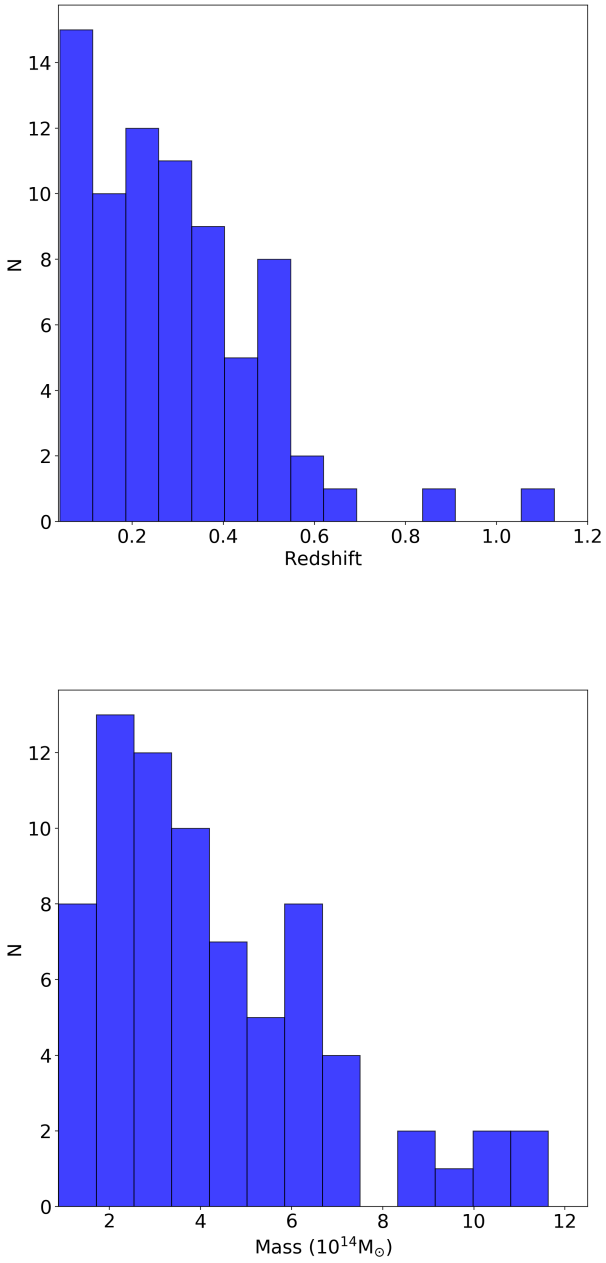

Fig. 1. Redshift and mass distribution of all clusters. *Upper panel*: histogram showing the redshift distribution of the sample. *Lower panel*: mass distribution of M_{500} of the cluster sample. The mass was estimated via the $L_X - M_{500}$ correlation from Chiu et al. (2022).

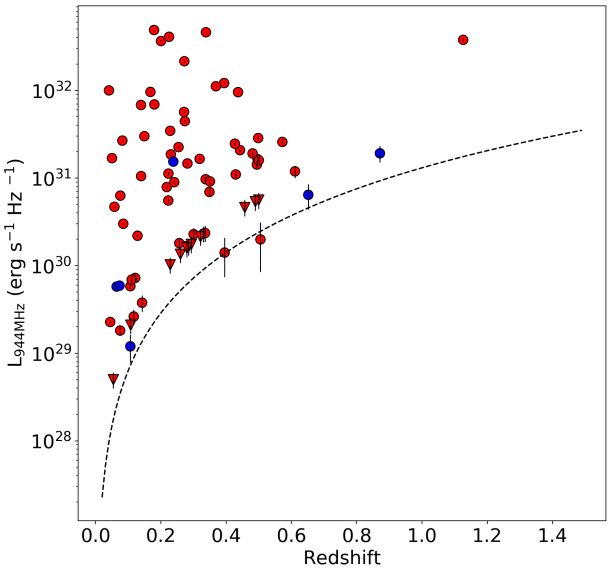

Fig. 2. 944 MHz radio luminosity vs. redshift. The dashed line represents the theoretical flux limit for point sources. The circles represent the clusters with a detected central radio source, and the triangles represent the upper limits. Resolved sources are plotted in red, and the blue points represent point sources.

Mountrichas et al. (2019) studied AGN in stripe 82 and showed that two-thirds of the X-ray detected AGN are not identified via the mid-infrared criterion. Especially AGN with luminosities between $10^{42.5} < L_X < 10^{44}$ erg s^{-1} are not detectable by the WISE criterion and show bluer $W1-W2$ colors. In this population, the AGN does not seem to dominate the mid-infrared emission, and therefore, the color criterion is not applicable to our sample, where most of our objects meet this luminosity.

3. Analysis and discussion

3.1. Linear size of the BCGs

Radio galaxies have a wide range of sizes and shapes, such as giant radio galaxies with largest linear sizes (LLS) of more than 0.7 Mpc, which were examined in Dabhade et al. (2020), for example, and small radio galaxies (e.g., Baldi et al. 2015). Hardcastle et al. (2019) examined the relation between radio power and the linear size of a sample of 23 344 radio-loud AGN, which is also referred to as the $P - D$ diagram (e.g., Turner et al. 2017). This diagram and the location of each source in it is an indicator for its initial conditions and its evolutionary state. The tracks of a source are associated with different phases in the evolution of the source. Objects with specific properties follow tracks on the plane that are mainly defined by the physics of the object. Remnant sources with switched-off jets describe a different set of tracks (Hardcastle 2018). However, the environment can also have an impact on the $P - D$ track. Sources in denser environments typically appear brighter than when they lie in more diluted environments (Turner & Shabala 2015; Yates-Jones et al. 2022).

We measured the angular sizes of the sources and then converted them into linear sizes using their redshift. The errors on the angular sizes were taken to be equal to the synthesized beam. The $P-D$ diagram for our sample is shown in Fig. 6. Pasini et al. (2022; P22 hereafter) examined a sample of 542 galaxy clusters and groups that were detected in the early performance verification phase (eFEDS) of eROSITA and compared them to the emission of the central radio galaxies detected with LOFAR. In Fig. 6 we compare the projected sizes of P22 to our data. To this end, we rescaled the 944 MHz luminosity to a luminosity at the LOFAR HBA central frequency of 144 MHz using a spectral index $\alpha = 0.6$. Our sample of eRASS:1 clusters extends the $P - D$ diagram to lower LLS values, with the luminosities being comparable to the luminosities $L_{144\,MHz}$ examined in P22, namely between $\sim 10^{23}$ and $\sim 10^{26}$ erg s^{-1} Hz^{-1}.

The EMU sample reaches similar radio powers as the LOFAR data because EMU reaches a depth of 25–30 μJy beam^{-1} at 944 MHz, which responds to a depth of 110 μJy beam^{-1} at the LOFAR frequency of 144 MHz, while the LOFAR observation of the eFEDS field reaches ∼100 μJy beam^{-1}. We also note that

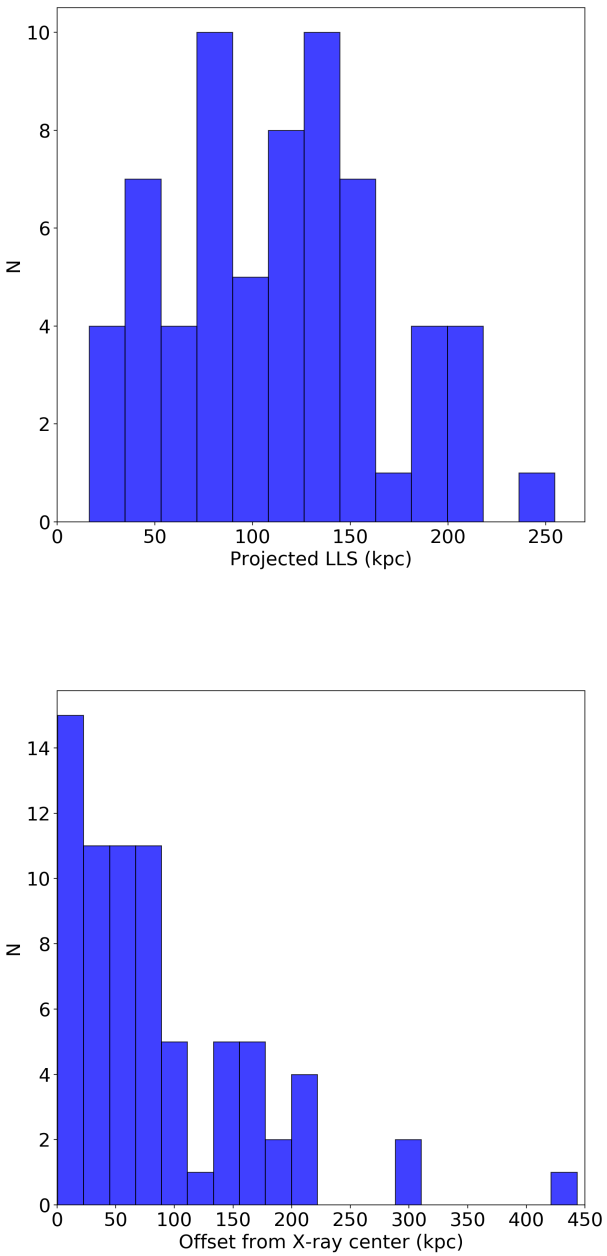

Fig. 3. Characteristics of the central radio sources. *Upper panel*: histogram showing the LLS in kiloparsec of each extended radio source. *Lower panel*: histogram showing the BCG offsets from the X-ray emission peak of the cluster.

the resolution of ASKAP is ∼18 arcsec, in contrast to LOFAR, which reaches ∼6 arcsec (Shimwell et al. 2017, 2019).

The interpretation of the $P - D$ diagram should be handled with care because several facts have to be taken into account. On the one hand, the environment and location within the cluster of the radio galaxy affects the position and track on the diagram. We also only observe the projected LLS, and we did not account for selection effects against large low-luminosity sources (Shabala et al. 2008; Turner & Shabala 2015). In addition, the redshift dependence might affect the $P - D$ diagram and its slope. We did not take the individual redshifts into account, which may result in a bias that distorts the true correlation between LLS and radio power. Different redshifts correspond to different cosmic epochs, in which the properties and evolutionary stages of radio galaxies can vary. Without a correction for redshift, objects at different redshifts may not be directly comparable. However, the correlation between the LLS and the radio luminosity is clearly positive: larger radio galaxies usually have higher radio luminosities.

In Fig. 7 we show the projected LLS versus 944 MHz radio power of the EMU radio galaxies. As previously observed, the correlation between LLS and luminosity is positive: larger radio galaxies are more powerful (Owen et al. 2002; Kolokythas et al. 2018; Pasini et al. 2022). The mean value of the LLS is 130 kpc, with a standard deviation of 74 kpc. We calculated the relation between the radio power and the LLS to be $\log P_{\rm R} = (3.12 \pm 0.1) \times \log \mathrm{LLS} - (17.33 \pm 0.22)$. Nonetheless, we note that we also expect a diagonal sensitivity limit because for a given luminosity of an extended source at a given redshift, larger sources are harder to detect because their surface brightness is lower (Shabala et al. 2008). For our sample, the theoretical cut-off limit does not play a role because it is four orders of magnitudes fainter that our measurements.

We also plot the projected LLS versus the central density of the ICM in Fig. 7. We conclude that these two observables are not correlated. However, color-coding the individual data points by the radio luminosity reveals that sources with a low central density and small LLS tend to exibit low radio luminosities. The lower central ICM density could imply a lower pressure in the radio lobes, leading to lower synchrotron emissivities, while smaller sources also favor lower luminosities.

3.2. BCG offset

In order to examine the BCG offset of each cluster, we calculated the physical distance between the X-ray center given in the eRASS:1 cluster catalog and the optically identified BCG. The result is shown in the lower panel of Fig. 3. The majority of BCGs are found within a radius of ∼100 kpc around the cluster center, which has been defined by the X-ray peak. This is consistent with the assumption of AGN feedback because the gas cooling out of the hot ICM can feed the central supermassive black hole (SMBH), while outer galaxies need to rely on more episodic triggers. Pasini et al. (2021) conducted a phase-space analysis by comparing the clustercentric velocity with the clustercentric offset of the hosted galaxies to investigate the assembly and accretion history of these objects. Their analysis suggests that powerful radio galaxies are always located close to the cluster center. The interpretation was that the cooling ICM can feed the AGN if the galaxy lies close to the cluster density peak, where the cooling is more efficient. Nonetheless, galaxies located in cluster outskirts can also host radio AGN, and triggers such as mergers or interactions might be important (Marshall et al. 2018). Small BCG offsets of less than 100 kpc are expected and found in most relaxed clusters because minor mergers can produce sloshing and displace the X-ray emission peak from the BCG (Hamer et al. 2016; Ubertosi et al. 2021). Larger offsets are usually an indication for major merger events, and therefore indicate strongly disturbed clusters (Hudson et al. 2010; Rossetti et al. 2016; De Propris et al. 2021; Ota et al. 2023; Seppi et al. 2023). In the next section, we compare the BCG offsets to the dynamical state of the clusters.

3.3. Morphological parameters

X-ray observations can be used to compute a quantitative measure of the dynamical status of a cluster. Different morphological parameters for quantifying the dynamical status of a cluster

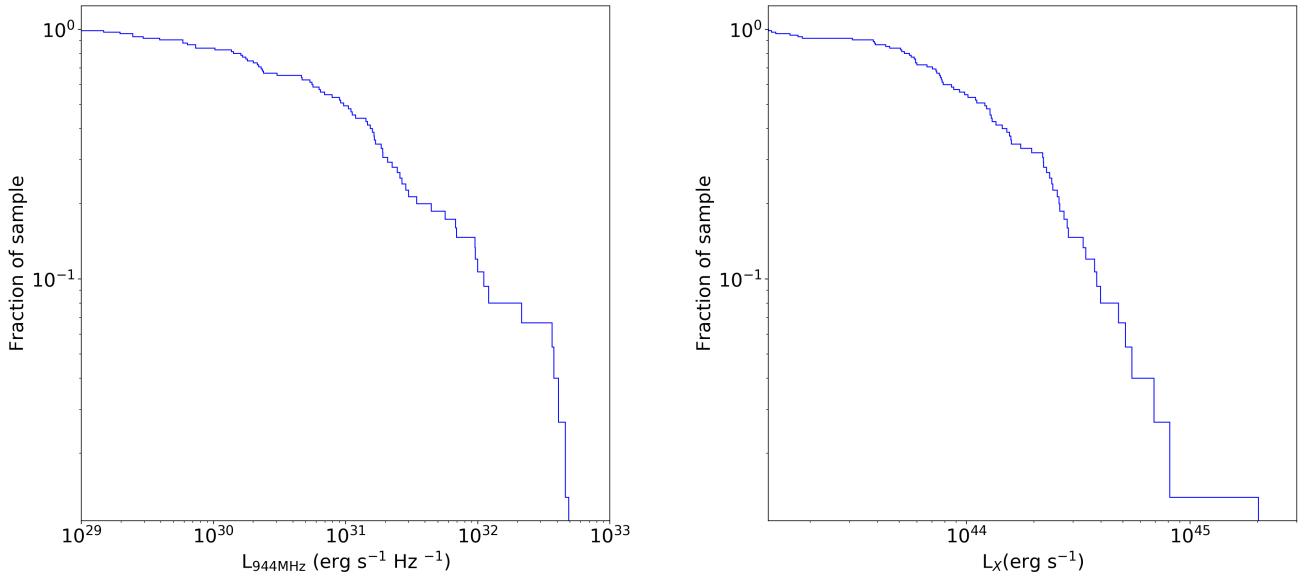

Fig. 4. Radio and X-ray luminosities of the cluster sample. *Left panel*: 944 MHz radio luminosity distribution for the cluster sample. *Right panel*: X-ray luminosity distribution in the sample for the 0.5–2.0 keV band.

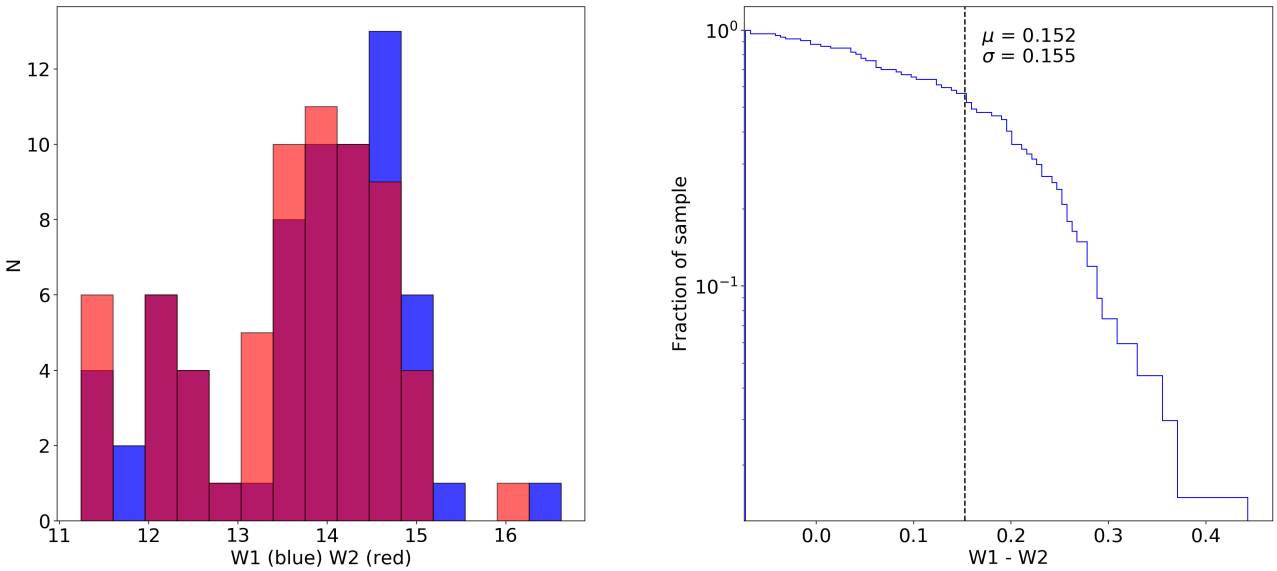

Fig. 5. WISE colors of the sample. *Left panel*: histogram showing the magnitude distribution of WISE colors $W1$ (blue) and $W2$ (red) in Vega magnitudes. *Right panel*: Distribution for $W1-W2$.

have been described in literature. We focus on the concentration parameter c. The concentration parameter is the ratio of the X-ray flux within a radius of 100 kpc around the cluster center to the X-ray flux within a radius of 500 kpc (Santos et al. 2008). It is defined as the ratio of the peak over the surface brightness S as

$$c \equiv \frac{S(r < 100\,\mathrm{kpc})}{S(r < 500\,\mathrm{kpc})}. \tag{3}$$

Clusters with a compact core that has not been disrupted by merger activity have higher concentration parameters. Hence, disturbed systems yield lower values for c. Cassano et al. (2010) and Bonafede et al. (2017) for example, have stated that considering the median value of $c = 0.2$, it is possible to distinguish between disturbed ($c < 0.2$) and more relaxed ($c > 0.2$) clusters. Figure 8 shows the plot of the concentration parameter against the BCG offset. Clusters that show a large offset from the BCG to the X-ray center clearly have concentration parameters of $c < 0.2$ and can thus be classified as disturbed systems. The link between the dynamical status of the clusters to their BCG offsets is clear, and larger offsets are found in more strongly disturbed systems.

Another commonly used morphological parameter is the power ratio P_3/P_0 (Buote & Tsai 1995). However, the number of photons in the eRASS:1 data is too low to yield a reliable estimate for the parameter P_3/P_0. We therefore will return to this in future work.

3.4. Correlation of the radio and X-ray luminosity

In this subsection, we investigate how the radio luminosity of the BCG relates to the global X-ray properties of the host cluster.

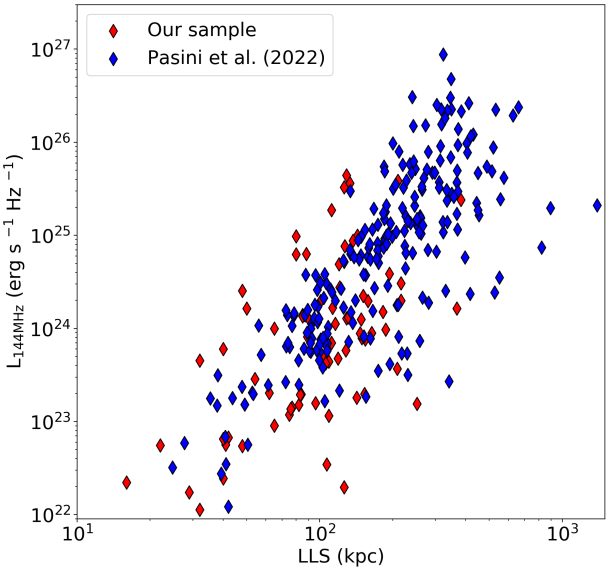

Fig. 6. Projected LLS vs. the 144 MHz luminosity from P21 and our sample. We rescaled the luminosity from 944 MHz to 144 MHz using the spectral index $\alpha = 0.6$.

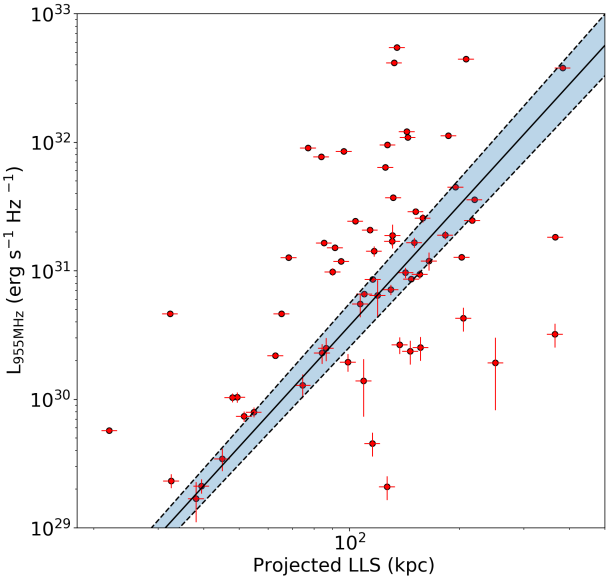

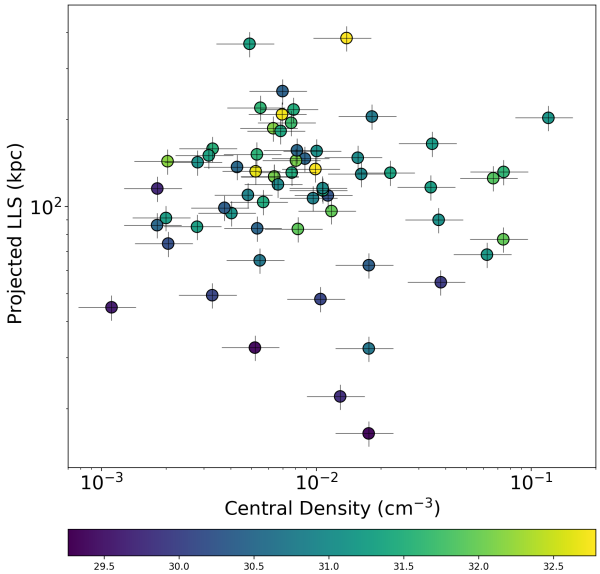

Fig. 7. Projected LLS vs. radio power and central density. *Upper panel*: projected LLS vs. 944 MHz radio power of the EMU radio galaxies. The black line represents the best fit, and the blue region inside the dashed lines is the error band: $\log P_R = (3.12 \pm 0.10) \times \log \mathrm{LLS} + (17.33 \pm 0.22)$. *Lower panel*: projected LLS of the radio source vs. the central density of the cluster. The data points are color-coded with the logarithmic radio luminosity in erg s^{-1} Hz^{-1}.

Figure 9 shows the 944 MHz luminosity of the central radio galaxy versus the X-ray luminosity of the galaxy cluster in the 0.1–2.4 keV band. The colors display the redshift, and the size of the points the LLS. There is a trend for more luminous radio galaxies to be hosted in more X-ray luminous clusters, but the scatter is significant. Using the Python package `hyperfit`[1], we calculated the correlation of the X-ray and radio luminosities (Robotham & Obreschkow 2015). This package provides a method for fitting a line to data allowing for both intrinsic scatter and (potentially correlated) errors on all the input variables, here x and y for our 2D fit. We ran this program on our data with a fully converged MCMC (Markov chain Monte Carlo) run. We obtained $\log L_R = (0.89 \pm 0.04) \times \log L_X - (8.52 \pm 1.44)$. The p-value of this fit equals 0.05. We therefore consider this relation to be statistically significant.

Clusters that host radio sources with high radio luminosities ($>5 \times 10^{31}$ erg s^{-1} Hz^{-1}) broaden the function and introduce large scatter into the correlation. A similar correlation was found by Hogan et al. (2015), even though they did not quantify their results. Our results are also consistent with the best-fit relation found by Pasini et al. (2022), who find $\log L_R = (0.84 \pm 0.09) \times \log L_X - (6.46 \pm 4.07)$ and Pasini et al. (2020, 2021). We refer to Table 2 for the corresponding relations. Although the results agree, our sample clearly has less scatter in the relation. One reason for this could be the large number of radio upper limits that were taken into account in former work. which adds larger uncertainties. Generally, we would expect more scatter at lower frequencies as lower frequencies are emitted by electrons that are older.

3.5. Mechanical powers of the jet

The radio lobes only radiate a small fraction of the total power away that is supplied to the lobes when the source is active. This small fraction of radiation is the radio luminosity, which is only a fraction of the energy produced by the AGN through accretion of matter toward the black hole itself. A larger fraction of the power is stored in the radio lobes and dissipated during the expansion of the jets into the ICM (Smolčić et al. 2017). A direct approach for calculating the mechanical power of a radio jet would be to derive it from the properties of the radio source in comparison with a radio source evolution model. In most cases, this is not possible because the radio environment of the sources is unknown. Moreover, the luminosity evolves with the age of the sources (Turner & Shabala 2015; Hardcastle 2018; Yates-Jones et al. 2022). A common approach to overcome this

[1] https://github.com/CullanHowlett/HyperFit

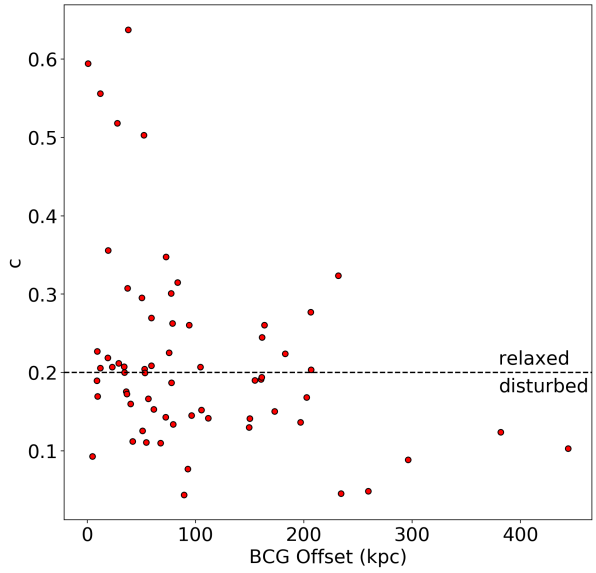

Fig. 8. Concentration parameter plotted vs. the BCG offset. The median value of $c = 0.2$ subdivides the sample into relaxed and disturbed clusters.

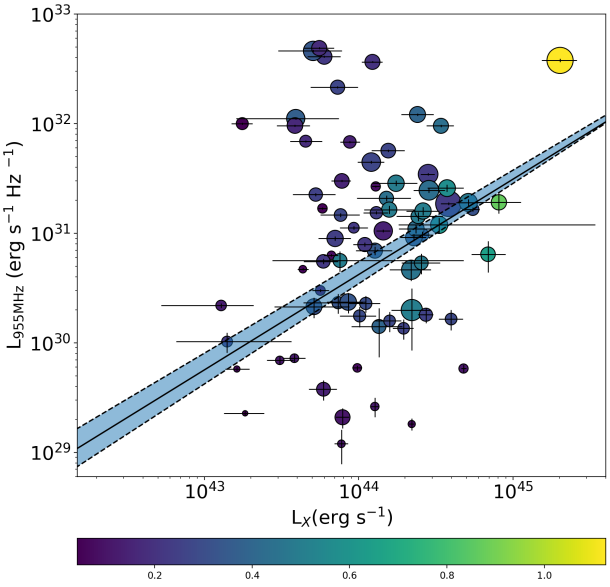

Fig. 9. 944 MHz luminosity of the central radio galaxy vs. the X-ray luminosity of the galaxy cluster in the 0.1–2.4 keV band. Each point is colored by redshift and scaled by the LLS. The black line represents the best fit, and the blue region inside the dashed lines shows the error band: $\log L_R = (0.89 \pm 0.04) \times \log L_X - (8.52 \pm 1.44)$.

problem is to estimate the mechanical energy of the jet by estimating it directly from the radio luminosity (Sabater et al. 2019).

This conversion of the mechanical power of the jet into radio luminosity is usually estimated from the cavities that are inflated by radio sources in the surrounding ICM as observed in X-ray images. The total mechanical energy is then calculated to $4pV$, with p the pressure of the surrounding medium, and V the volume of the cavity. The factor of 4 arises if the enthalpy of the relativistic plasma in the radio lobes, which is $3pV$, is added to the work performed to inflate the cavities, which is pV. When an estimate of the source age (e.g., via the buoyancy timescale of the cavity) is also given, a lower limit of the mechanical power of the jet can be estimated. This is found to correlate with the observed radio luminosity (Rafferty et al. 2006; Bîrzan et al. 2008; Cavagnolo et al. 2010).

Another approach to relate the mechanical power of the jet to the radio luminosity is based on the synchrotron properties, and therefore, on the composition of the jet plasma (Willott et al. 1999). Heckman & Best (2014) found that both approaches provide consistent estimates of the mechanical powers of the jet and proposed a population-averaged conversion,

$$P_{\mathrm{mech,cav}} = 2.8 \times 10^{37} \left(\frac{L_{1.4\,\mathrm{GHz}}}{10^{25}\,\mathrm{WHz}^{-1}} \right)^{0.68} \mathrm{W}.$$

Furthermore, the kinetic luminosity at a rest-frame frequency of 1.4 GHz is described by

$$\log L_{\mathrm{kin,1.4\,GHz}} = 0.86 \log L_{1.4\,\mathrm{GHz}} + 14.08 + 1.5 \log f_W.$$

$L_{\mathrm{kin,1.4\,GHz}}$ describes the kinetic luminosity, and $L_{1.4\,\mathrm{GHz}}$ is the luminosity at 1.4 GHz. f_W is an uncertainty parameter, which is estimated to be around 15 from observations (Smolčić et al. 2017). In order to determine the kinetic luminosity for our sample, we converted the radio power at 944 MHz to radio powers at a frequency of 1.4 GHz, assuming a spectral index of $\alpha = 0.6$. We then compared our results to the X-ray luminosity of the host cluster. We again used the package `hyperfit` to estimate our relation in log-log scale in the form

$$Y = \alpha + \beta X + \varepsilon,$$

where α and β represent the intercept and slope, and ε is the intrinsic scatter. We find $\alpha = -3.81 \pm 1.01, \beta = 1.08 \pm 0.03$, and $\varepsilon = 0.91 \pm 0.61$ (see Fig. 10). This approximately agrees with the values found by Pasini et al. (2022), who found $\alpha = -2.19 \pm 4.05, \beta = 1.07 \pm 0.11$, and $\varepsilon = 0.25 \pm 0.05$. However, we obtain a larger ε-factor for our sample, which represents a higher uncertainty in the observed values. As the conversion from the 944 MHz luminosity into kinetic luminosity at 1.4 GHz depends on a number of assumptions, we introduced large errors that result in a high scatter of the relation. Moreover, our sample is smaller than that of P22, which also results in a higher scatter. We also note that considering a sample over a wide redshift range can introduce a bias into this estimation (Godfrey & Shabala 2016). Previous results from P22 stating that in most clusters the heating from the central AGN balances the ICM radiative losses cannot be confirmed from our data (see also, e.g., McNamara & Nulsen 2012; McNamara et al. 2016 for a review). However, we note that P22 used additional COSMOS data of lower-luminosity galaxy groups than the initial eFEDS data (see their Fig. 10). When the COSMOS data are removed from their data, their correlation between the kinetic luminosity at 1.4 GHz and L_X also becomes far lower. The scatter in the radio luminosity appears to increase strongly with L_X, similar to the results of Main et al. (2017). At values $L_X > 10^{43}$ erg s^{-1}, the correlation disappears. The kinetic luminosity acts as a proxy for the heating rate, and the X-ray luminosity acts as a proxy for the cooling rate. Hence, the central AGN appear to counterbalance radiative losses from the ICM in low-luminosity clusters and groups, but this relation breaks for high-luminosity clusters. Main et al. (2017) also investigated this relation and reported that the correlation between kinetic luminosity and X-ray observables only holds in clusters with short (<1 Gyr) central cooling times. We derived the central cooling time t_{cool} based on the X-ray temperature and color-code the individual points with respect to t_{cool} in Fig. 10 to examine whether t_{cool} affects the individual cluster position in the $L_{\mathrm{kin}} - L_X$ diagram.

Table 2. Overview of the X-ray/radio correlation found by other authors.

Author	Sources	z	M	Correlation
(Mittal et al. 2009)	64	0.0037–0.2153	$10^{13} < M_{\odot} < 10^{14}$	$\log L_{\rm R} = (1.38 \pm 0.16) \times \log L_{\rm X} - (1.52 \pm 0.3)$
(Pasini et al. 2020)	247	0.08–1.75	$10^{13} < M_{\odot} < 10^{14}$	$\log L_{\rm R} = (1.07 \pm 0.12) \times \log L_{\rm X} - (15.90 \pm 5.13)$
(Pasini et al. 2021)	79	0.08–1.53	$8 \times 10^{12} < M_{\odot} < 3 \times 10^{14}$	$\log L_{\rm R} = (0.94 \pm 0.43) \times \log L_{\rm X} - (9.53 \pm 18.19)$
(Pasini et al. 2022)	542	0.1–1.3	$3.4 \times 10^{12} < M_{\odot} < 6.4 \times 10^{14}$	$\log L_{\rm R} = (0.84 \pm 0.09) \times \log L_{\rm X} - (6.46 \pm 4.07)$
This work	75	0.03–1.1	$10^{13} < M_{\odot} < 10^{15}$	$\log L_{\rm R} = (0.89 \pm 0.04) \times \log L_{\rm X} - (8.52 \pm 1.44)$

We cannot confirm the results from Main et al. (2017) based on our data. In high-luminosity clusters, the variability among the AGN population seems to be higher, resulting in a higher scatter in the $L_{\rm kin} - L_{\rm X}$ correlation. However, the measurements are only a snapshot in the lifetime of an AGN at a certain point in their duty cycle. Averaged over a longer period, AGN heating could still balance cooling, but the implication is that at higher $L_{\rm X}$, the AGN are more variable.

3.6. Cooling time

Because AGN feedback heats the ICM and regulates its cooling rate, the correlation between central cooling time and radio luminosity can be used to investigate the relation between ICM cooling and AGN heating. Because the eRASS:1 cluster catalog provides the central density $n_{\rm e}$ and the temperature $T_{\rm X}$ for all clusters, the central cooling time can be approximated as (Sarazin 1986)

$$t_{\rm cool} = 8.5 \times 10^{10}\,{\rm yr}\left(\frac{n_P}{10^{-3}\,{\rm cm}^{-3}}\right)^{-1}\left(\frac{T_{\rm g}}{10^{8}\,{\rm K}}\right)^{\frac{1}{2}}.$$

We assumed a hydrogen density $n_P = 0.83 n_{\rm e}$ (McDonald et al. 2018). We plot the cooling time $t_{\rm cool}$ versus the radio luminosity $L_{\rm R}$ in the right panel of Fig. 10. We removed two outliers with derived central cooling times of $>10^{12}$ yr because these values are most likely the result of incorrect densities and temperatures in the catalog data. While the plot is messy, there seems to be a trend of an anticorrelation between the two quantities. To quantify this anticorrelation, we find $\log L_{\rm R} = (-0.31 \pm 0.03) \times \log t_{\rm cool} + (34.17 \pm 0.31)$. We also indicate $t_{\rm cool} = 7.7$ Gyr because this value is commonly used to distinguish between cool-core (CC) and non-cool-core clusters (NCC). Our sample contains 10 CC clusters, while the rest are NCC clusters. Mittal et al. (2009) examined a sample of 64 HIFLUGCS clusters and their central radio galaxies and found a similar trend for an anticorrelation between the cooling time of the cluster and the radio luminosity of its central AGN. For their sample, they reported a slope of -3.16 ± 0.38, which is in contrast to our relation, where we find a slope of -0.31 ± 0.03. We note that Mittal et al. (2009) used a central definition of 0.4% of r_{500}, which is a radius that cannot be resolved by eROSITA. Hence, any comparison should be handled with care. In general, this apparent anticorrelation could be indicative of a need for more powerful AGN in clusters with short central cooling times. Cool-core clusters with very short cooling times seem to need much more powerful AGN, unlike NCC clusters, in which this trend is less obvious. Finally, the cluster mass also appears to play a role. Bharadwaj et al. (2014) investigated the same relation for galaxy groups and found no relation between the central cooling time and the radio luminosity of the central AGN. For a discussion of the difference of AGN feedback in clusters and groups, we refer to Pasini et al. (2021).

3.7. Density profiles

In order to investigate the connection between CC and NCC clusters and their corresponding radio luminosity, we plot the density profiles of all clusters of our sample and color-code them by their radio power. The resulting plot is shown in Fig. 11. We again removed the density profiles of two outliers with very low central densities of $n_{\rm e} < 10^{-4}$ because we assume that these values are incorrect. Clusters with a higher central density ($n_{\rm e} > 10^{-2}\,{\rm cm}^{-3}$), subsequently CC clusters, tend to host more luminous radio sources with radio luminosities of $L_{\rm R} > 10^{31}\,{\rm erg\,s^{-1}\,Hz^{-1}}$. This confiRMS that CC clusters always host a powerful radio-mode AGN. Clusters with lower central densities ($n_{\rm e} < 10^{-2}\,{\rm cm}^{-3}$) show no connection, and we draw the conclusion that NCC clusters host low- as well as high-luminous radio sources. This agrees overall with the general findings that X-ray cavities and therefore powerful radio-mode AGN are usually found within CC clusters (e.g., O'Sullivan et al. 2011; Hlavacek-Larrondo et al. 2012; Bîrzan et al. 2020; Olivares et al. 2022). In contrast to this strong connection of AGN activity and CC clusters, NCC clusters and AGN activity do not appear to be correlated. Mittal et al. (2009) showed that NCC clusters may also host strong radio AGN, which can be explained by merging activities or other mechanisms, for instance.

3.8. Noteworthy clusters

Our cluster sample contains some interesting radio sources, four of which are presented in Fig. 12. The upper left panel shows galaxy cluster J201832.9-524656 (Abell S0861) at $z = 0.05$. The white circle is R_{500}. This cluster contains two interesting radio sources with very elongated shapes. We also show the overlay with optical data from the legacy survey DR9, in which the upper radio source presumably consists of at least three galaxies exhibiting radio emission. The shape of the radio emission suggests a complex interplay between these galaxies. The southern radio source in J201832.9-524656 resembles the shape of a jellyfish galaxy. The optical overlay shows a bright galaxy in the upper part of the radio galaxy. This shape suggests that this galaxy is moving northwest.

The upper right panel of Fig. 12 shows cluster J205156.7-523752 (PLCKESZ G345.4-39) at $z = 0.04$. This cluster hosts two elongated radio sources in the southern part of the cluster that seem to be connected. The optical overlay with legacy survey DR9 data reveals that the upper radio source consists of two near galaxies, and the upper radio source is at least one radio galaxy. The shapes of these sources suggest that these galaxies have either undergone some merging activities in the past or will do so in the future. In the lower left panel, we display cluster J202321.7-553524 (SPT-CL J2023-5535) at $z = 0.22$. The radio image of this cluster reveals a radio source that

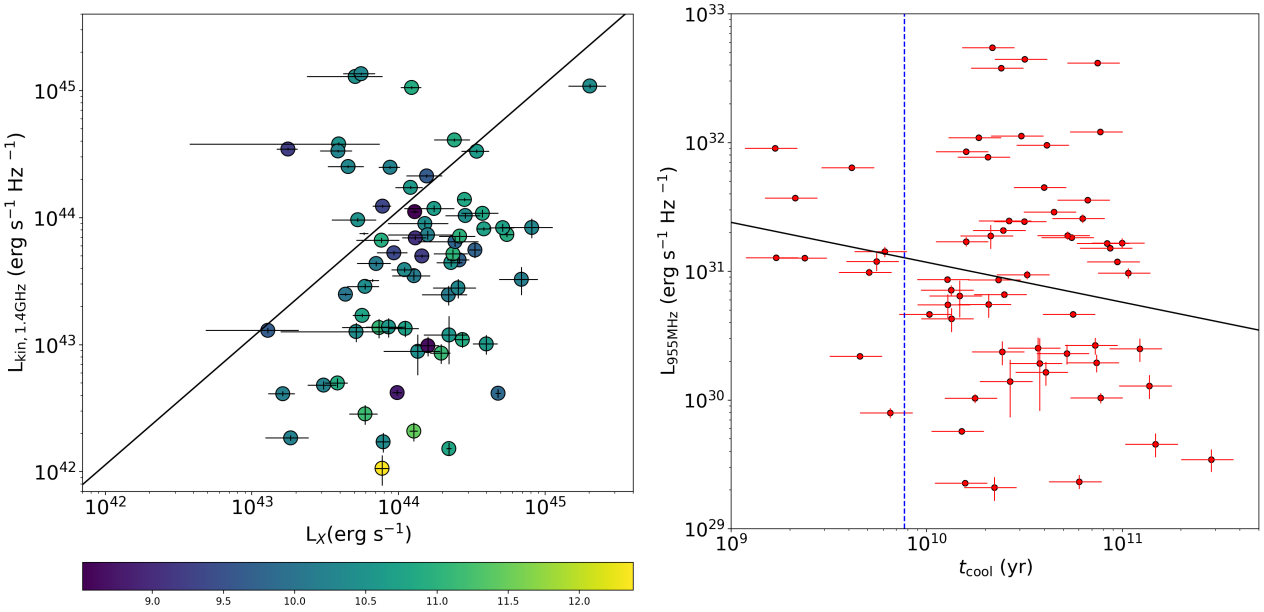

Fig. 10. X-ray luminosity of the clusters sample vs. the corresponding radio luminosity of the central radio source and the 944 MHz radio luminosity of the central radio source vs. the central cooling time of each cluster. *Left panel*: 1.4 GHz kinetic luminosity extrapolated from 944 MHz vs. the X-ray luminosity of the corresponding cluster. The individual points are color-coded with respect to the logarithmic central cooling time. *Right panel*: 944 MHz radio luminosity of the central radio source vs. the central cooling time of each cluster. The vertical dashed blue line indicates t_{cool} = 7.7 Gyr and separates CC and NCC clusters. The black line indicates the fit: $\log L_R = (-0.31 \pm 0.03) \times \log t_{cool} + (34.17 \pm 0.31)$.

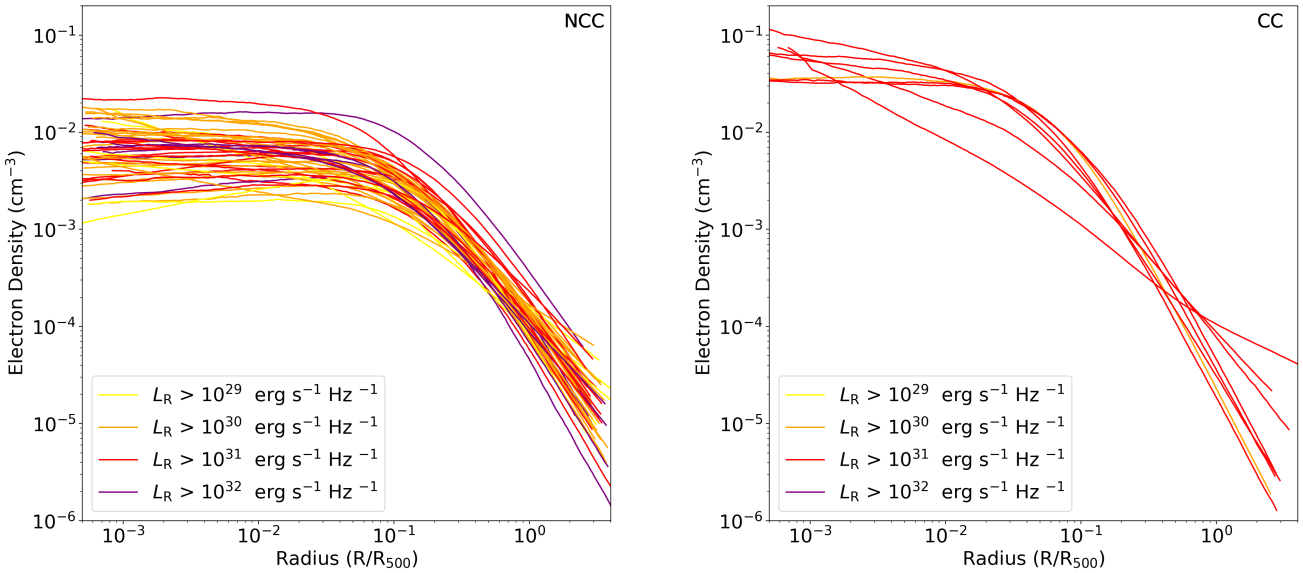

Fig. 11. Electron density profiles of the cluster sample. *Left panel*: electron density profiles of all non-cool-core clusters vs. the radius scaled to R_{500}. The colors of the profiles represent the radio luminosity of the central radio source of the corresponding cluster. *Right panel*: corresponding plot for the cool-core clusters.

covers large areas of the whole cluster, with a strong peak in the southeast. This radio source could be an indication for a radio halo and has also been studied by HyeongHan et al. (2020). In the lower right panel, we display the nearby cluster J215129.7-552019 (RXC J2151.3-5521) at z = 0.03. The radio jets clearly originate from the central radio source in the cluster.

4. Conclusions

We used the eROSITA eRASS:1 cluster catalog and the ASKAP pilot survey EMU to examine the central radio galaxies hosted in galaxy clusters covered in the EMU survey. We can draw the following conclusions:

– Our sample consists of 75 galaxy clusters that are covered by the EMU pilot survey in the redshift range of 0.03 < z < 1.1. Ten clusters are cool-core clusters, while the rest are non-cool-core clusters. In 64 clusters we could identify a radio source that corresponds to the cluster BCG. The radio luminosities of the central radio galaxies at 944 MHz range between ∼10^{29} and ∼10^{33} erg s^{-1} Hz^{-1}. The X-ray luminosities of the corresponding clusters range between ∼10^{43} and ∼10^{45} erg s^{-1}.

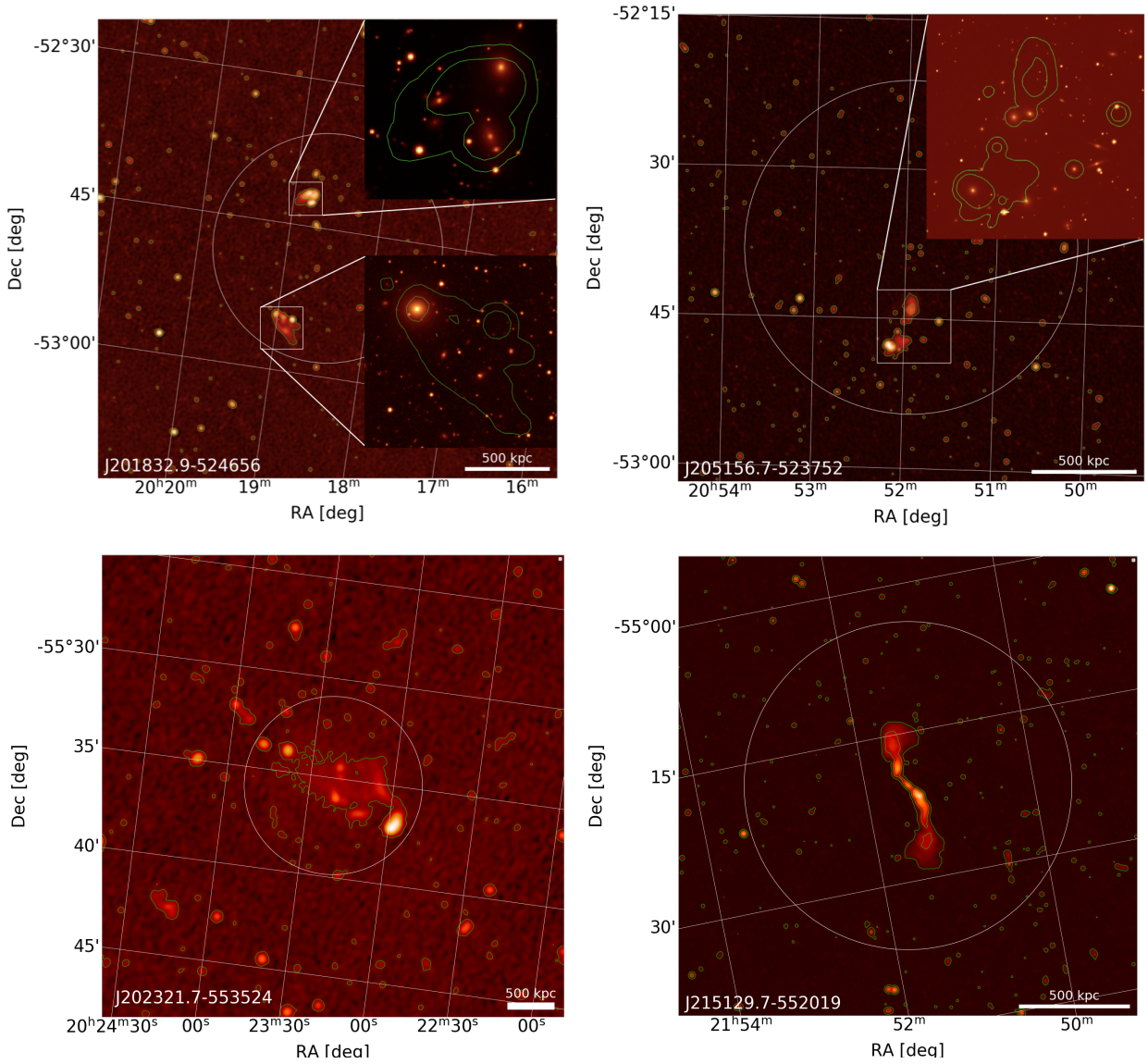

Fig. 12. Special radio sources contained in the EMU field. *Upper left panel*: radio cutout from the EMU image of cluster J201832.9-524656 (Abell S0861) at $z = 0.05$ showing two elongated radio sources. The optical overlay reveals a complex interplay between at least three radio galaxies on the northern radio source and an infalling radio galaxy in the southern source. *Upper right panel*: the radio cutout of J205156.7-523752 (PLCKESZ G345.4-39) at $z = 0.04$ shows two connected elongated radio sources that seem to be hosted by at least three radio galaxies. *Lower left panel*: radio image of J202321.7-553524 (SPT-CL J2023-5535) at $z = 0.22$ revealing a large radio source. *Lower right panel*: cutout of the nearby cluster J215129.7-552019 (RXC J2151.3-5521) at $z = 0.03$ clearly showing the radio jets that originate from the central radio source. All optical overlays made use of legacy survey DS9 data, and the white circle represents R_{500}.

– We compared the offset of the BCG from the cluster center to its concentration parameter. We found a link between the dynamical state of the cluster to its BCG offset. Larger offsets were found in more strongly disturbed systems.
– We find a statistically significant correlation between the radio and the X-ray luminosity, as in previous work (Mittal et al. 2009; Pasini et al. 2020, 2021, 2022).
– We investigated the correlation between the LLS of the radio source and its radio power, finding that larger radio galaxies tend to be more powerful. We do not find a correlation between the central density and the LLS, which suggests that the radio power is more important than the ambient density for the size of the radio galaxy.
– The 944 MHz luminosities were converted into 1.4 GHz kinetic luminosities using scaling relations. We found that in high-luminosity clusters with $L_X > 10^{43}$ erg s^{-1}, the kinetic luminosity of the radio jets is not longer correlated with the X-ray luminosity. This indicates that the variability in the AGN population is higher in high luminous clusters.
– We found an anticorrelation between the central cooling time t_{cool} and the radio luminosity L_R, indicating that more powerful AGN reside in clusters with short central cooling times.
– The density profiles of the individual clusters show that cool-core clusters tend to host powerful radio sources, in contrast to non-cool-core clusters, which host both high- and low-luminosity radio sources.
– A mid-infrared color criterion using WISE colors was applied to our sample. We conclude that the color criterion is not applicable for our sample, which is due to the luminosity range of our sample, for which the WISE criterion is not applicable.

The eRASS cluster catalog is a powerful tool that will prove useful for future studies. The combination with radio surveys by the forthcoming generation of radio telescopes will vastly extend samples such as ours.

Acknowledgements. The authors thank the anonymous referee for useful comments and suggestions. The Australian SKA Pathfinder is part of the Australia Telescope National Facility which is managed by CSIRO. Operation of ASKAP is funded by the Australian Government with support from the National Collaborative Research Infrastructure Strategy. ASKAP uses the resources of the Pawsey Supercomputing center. Establishment of ASKAP, the Murchison Radio-astronomy Observatory and the Pawsey Supercomputing center are initiatives of the Australian Government, with support from the Government of Western Australia and the Science and Industry Endowment Fund. We acknowledge the Wajarri Yamatji people as the traditional owners of the Observatory site. The Australia Telescope Compact Array (/Parkes radio telescope/Mopra radio telescope/Long Baseline Array) is part of the Australia Telescope National Facility which is funded by the Australian Government for operation as a National Facility managed by CSIRO. This paper includes archived data obtained through the Australia Telescope Online Archive (http://atoa.atnf.csiro.au). This work was supported by resources provided by the Pawsey Supercomputing center with funding from the Australian Government and the Government of Western Australia. We acknowledge and thank the builders of ASKAPsoft. This work is based on data from eROSITA, the soft X-ray instrument aboard SRG, a joint Russian-German science mission supported by the Russian Space Agency (Roskosmos), in the interests of the Russian Academy of Sciences represented by its Space Research Institute (IKI), and the Deutsches Zentrum für Luft- und Raumfahrt (DLR). The SRG spacecraft was built by Lavochkin Association (NPOL) and its subcontractors, and is operated by NPOL with support from the Max Planck Institute for Extraterrestrial Physics (MPE). The development and construction of the eROSITA X-ray instrument was led by MPE, with contributions from the Dr. Karl Remeis Observatory Bamberg and ECAP (FAU Erlangen-Nuernberg), the University of Hamburg Observatory, the Leibniz Institute for Astrophysics Potsdam (AIP), and the Institute for Astronomy and Astrophysics of the University of Tübingen, with the support of DLR and the Max Planck Society. The Argelander Institute for Astronomy of the University of Bonn and the Ludwig Maximilians Universität Munich also participated in the science preparation for eROSITA. This publication makes use of data products from the Wide-field Infrared Survey Explorer, which is a joint project of the University of California, Los Angeles, and the Jet Propulsion Laboratory/California Institute of Technology, funded by the National Aeronautics and Space Administration. KB and MB are funded by the Deutsche Forschungsgemeinschaft (DFG, German Research Foundation) under Germany's Excellence Strategy - EXC 2121 "Quantum Universe" – 390833306.

References

Assef, R. J., Kochanek, C. S., Brodwin, M., et al. 2010, ApJ, 713, 970
Assef, R. J., Stern, D., Noirot, G., et al. 2018, ApJS, 234, 23
Baldi, R. D., Capetti, A., & Giovannini, G. 2015, A&A, 576, A38
Bharadwaj, V., Reiprich, T. H., Schellenberger, G., et al. 2014, A&A, 572, A46
Bîrzan, L., Rafferty, D. A., McNamara, B. R., Wise, M. W., & Nulsen, P. E. J. 2004, ApJ, 607, 800
Bîrzan, L., McNamara, B. R., Nulsen, P. E. J., Carilli, C. L., & Wise, M. W. 2008, ApJ, 686, 859
Bîrzan, L., Rafferty, D. A., Brüggen, M., et al. 2020, MNRAS, 496, 2613
Bonafede, A., Cassano, R., Brüggen, M., et al. 2017, MNRAS, 470, 3465
Brunner, H., Liu, T., Lamer, G., et al. 2022, A&A, 661, A1
Buote, D. A., & Tsai, J. C. 1995, ApJ, 452, 522
Cassano, R., Ettori, S., Giacintucci, S., et al. 2010, ApJ, 721, L82
Cattaneo, A., Faber, S. M., Binney, J., et al. 2009, Nature, 460, 213
Cavagnolo, K. W., McNamara, B. R., Nulsen, P. E. J., et al. 2010, ApJ, 720, 1066
Chiu, I. N., Ghirardini, V., Liu, A., et al. 2022, A&A, 661, A11
Condon, J. J., Cotton, W. D., & Broderick, J. J. 2002, AJ, 124, 675
Dabhade, P., Röttgering, H. J. A., Bagchi, J., et al. 2020, A&A, 635, A5
De Propris, R., West, M. J., Andrade-Santos, F., et al. 2021, MNRAS, 500, 310
Fabian, A. 2012, ARA&A, 50, 455
Gaspari, M., Tombesi, F., & Cappi, M. 2020, Nat. Astron., 4, 10
Gitti, M., Brighenti, F., & McNamara, B. R. 2012, Adv. Astron., 2012, 1
Godfrey, L. E. H., & Shabala, S. S. 2016, MNRAS, 456, 1172
Guzman, J., Whiting, M., Voronkov, M., et al. 2019, Astrophysics Source Code Library [record ascl:1912.003]
Hamer, S. L., Edge, A. C., Swinbank, A. M., et al. 2016, MNRAS, 460, 1758
Hardcastle, M. J. 2018, MNRAS, 475, 2768
Hardcastle, M. J., Williams, W. L., Best, P. N., et al. 2019, A&A, 622, A12
Heckman, T. M., & Best, P. N. 2014, ARA&A, 52, 589
Hlavacek-Larrondo, J., Fabian, A. C., Edge, A. C., et al. 2012, MNRAS, 421, 1360
Hogan, M. T., Edge, A. C., Hlavacek-Larrondo, J., et al. 2015, MNRAS, 453, 1201
Hopkins, A. M., Whiting, M. T., Seymour, N., et al. 2015, PASA, 32, 23
Hotan, A. W., Bunton, J. D., Chippendale, A. P., et al. 2021, PASA, 38, e009
Hudson, D. S., Mittal, R., Reiprich, T. H., et al. 2010, A&A, 513, A37
HyeongHan, K., Jee, M. J., Rudnick, L., et al. 2020, ApJ, 900, 127
Ineson, J., Croston, J. H., Hardcastle, M. J., et al. 2013, ApJ, 770, 136
Ineson, J., Croston, J. H., Hardcastle, M. J., et al. 2015, MNRAS, 453, 2682
Johnston, S., Taylor, R., Bailes, M., et al. 2008, Exp. Astron., 22, 151
Kolokythas, K., O'Sullivan, E., Raychaudhury, S., et al. 2018, MNRAS, 481, 1550
Koribalski, B. S. 2022, in 2022 3rd URSI Atlantic and Asia Pacific Radio Science Meeting (AT-AP-RASC), 1
LaMassa, S. M., Georgakakis, A., Vivek, M., et al. 2019, ApJ, 876, 50
Liu, A., Bulbul, E., Ghirardini, V., et al. 2022, A&A, 661, A2
Magliocchetti, M., & Brüggen, M. 2007, MNRAS, 379, 260
Main, R. A., McNamara, B. R., Nulsen, P. E. J., Russell, H. R., & Vantyghem, A. N. 2017, MNRAS, 464, 4360
Marshall, M. A., Shabala, S. S., Krause, M. G. H., et al. 2018, MNRAS, 474, 3615
Mauch, T., & Sadler, E. M. 2007, MNRAS, 375, 931
McDonald, M., Gaspari, M., McNamara, B. R., & Tremblay, G. R. 2018, ApJ, 858, 45
McNamara, B. R., & Nulsen, P. E. J. 2012, New J. Phys., 14, 055023
McNamara, B. R., Russell, H. R., Nulsen, P. E. J., et al. 2016, ApJ, 830, 79
Merloni, A., Predehl, P., Becker, W., et al. 2012, ArXiv e-prints [arXiv:1209.3114]
Merloni, A., Nandra, K., & Predehl, P. 2020, Nat. Astron., 4, 634
Mittal, R., Hudson, D. S., Reiprich, T. H., & Clarke, T. 2009, A&A, 501, 835
Mountrichas, G., Georgantopoulos, I., Ruiz, A., & Kampylis, G. 2019, MNRAS, 491, 1727
Nipoti, C., & Binney, J. 2005, MNRAS, 361, 428
Norris, R. P., Hopkins, A. M., Afonso, J., et al. 2011, PASA, 28, 215
Norris, R. P., Marvil, J., Collier, J. D., et al. 2021, PASA, 38, e046
Olivares, V., Su, Y., Nulsen, P., et al. 2022, MNRAS, 516, L101
O'Sullivan, E., Giacintucci, S., David, L. P., et al. 2011, ApJ, 735, 11
Ota, N., Nguyen-Dang, N. T., Mitsuishi, I., et al. 2023, A&A, 669, A110
Owen, F., Ledlow, M., & Eilek, J. 2002, Highlights Astron., 12, 522
Pasini, T., Brüggen, M., de Gasperin, F., et al. 2020, MNRAS, 497, 2163
Pasini, T., Finoguenov, A., Brüggen, M., et al. 2021, MNRAS, 505, 2628
Pasini, T., Brüggen, M., Hoang, D. N., et al. 2022, A&A, 661, A13
Pope, E. C. D., Mendel, J. T., & Shabala, S. S. 2012, MNRAS, 419, 50
Predehl, P., Andritschke, R., Arefiev, V., et al. 2021, A&A, 647, A1
Rafferty, D. A., McNamara, B. R., Nulsen, P. E. J., & Wise, M. W. 2006, ApJ, 652, 216
Robotham, A. S. G., & Obreschkow, D. 2015, PASA, 32, e033
Rossetti, M., Gastaldello, F., Ferioli, G., et al. 2016, MNRAS, 457, 4515
Sabater, J., Best, P. N., Hardcastle, M. J., et al. 2019, A&A, 622, A17
Sadler, E. M., Jackson, C. A., Cannon, R. D., et al. 2002, MNRAS, 329, 227
Santos, J. S., Rosati, P., Tozzi, P., et al. 2008, A&A, 483, 35
Sarazin, C. L. 1986, Rev. Mod. Phys., 58, 1
Scott, K. S., Austermann, J. E., Perera, T. A., et al. 2008, MNRAS, 385, 2225
Seppi, R., Comparat, J., Nandra, K., et al. 2023, A&A, 671, A57
Shabala, S. S., Ash, S., Alexander, P., & Riley, J. M. 2008, MNRAS, 388, 625
Shabala, S. S., Jurlin, N., Morganti, R., et al. 2020, MNRAS, 496, 1706
Shimwell, T. W., Röttgering, H. J. A., Best, P. N., et al. 2017, A&A, 598, A104
Shimwell, T. W., Tasse, C., Hardcastle, M. J., et al. 2019, A&A, 622, A1
Smolčić, V., Delvecchio, I., Zamorani, G., et al. 2017, A&A, 602, A2
Stern, D., Assef, R. J., Benford, D. J., et al. 2012, ApJ, 753, 30
Sunyaev, R., Arefiev, V., Babyshkin, V., et al. 2021, A&A, 656, A132
Timmerman, R., van Weeren, R.J., Botteon, A., et al. 2022, A&A, 668, A65
Turner, R. J., & Shabala, S. S. 2015, ApJ, 806, 59
Turner, R. J., Rogers, J. G., Shabala, S. S., & Krause, M. G. H. 2017, MNRAS, 473, 4179
Ubertosi, F., Gitti, M., Torresi, E., Brighenti, F., & Grandi, P. 2021, MNRAS, 503, 4627
Whiting, M., Voronkov, M., Mitchell, D., & Askap Team 2017, ASP Conf. Ser., 512, 431
Wieringa, M., Raja, W., & Ord, S. 2020, ASP Conf. Ser., 527, 591
Willott, C. J., Rawlings, S., Blundell, K. M., & Lacy, M. 1999, MNRAS, 309, 1017
Wright, E. L., Eisenhardt, P. R. M., Mainzer, A. K., et al. 2010, AJ, 140, 1868
Yates-Jones, P. M., Turner, R. J., Shabala, S. S., & Krause, M. G. H. 2022, MNRAS, 511, 5225

Appendix A: eRASS:1 clusters in the EMU field

We show a table of all eRASS:1 detected clusters in the EMU field and their corresponding X-ray characteristics. The radio values of the corresponding central radio source are also listed.

Table A.1. eRASS:1 clusters in the EMU field and their corresponding values.

Cluster ID	RA	DEC	z	S_{Radio} (mJy)	LLS (kpc)	L_X (10^{43} erg s^{-1})	M ($10^{14}M_\odot$)	r_{500}	n_e (cm^{-3})	BCG ID
J201601.3-495436	304.006	-49.910	0.271	28.652	120	15.562	4.654	1075	0.067	J201601.62-495445.5
J201847.9-524238	304.700	-52.711	0.050	290.843	50	5.826	2.581	953	0.361	2MASX J20184669-5241274
J202154.3-525715	305.476	-52.954	0.139	142.582	88	8.768	3.295	1004	0.012	J202147.81-525705.2
J202321.7-553524	305.840	-55.590	0.231	13.325	368	38.238	8.796	1349	0.005	[GSB2009] J202320.83-553549.9
J203328.8-593552	308.370	-59.598	0.200	353.543	126	12.290	4.099	1057	0.005	J203331.05-593549.4
J202555.3-511709	306.481	-51.286	0.229	25.188	216	28.201	7.165	1260	0.005	2MASX J20255579-5116276
J202726.9-522215	306.862	-52.371	0.064	5.976	22	1.624	1.066	707	0.013	6dFGS gJ202728.4-522210
J203601.2-513931	309.005	-51.659	0.272	107.958	112	7.305	2.763	903	0.017	WISEA J203557.84-513909.5
J203220.5-562738	308.086	-56.461	0.284	0.750	77	39.745	8.832	1324	0.005	[GSB2009] J203223.81-562759.4
J203043.7-563749	307.682	-56.630	0.394	27.148	143	24.071	5.940	1113	0.002	[BRS2016] J203045.25-563755.8
J204612.1-575544	311.551	-57.929	0.225	308.326	133	5.985	2.445	882	0.043	WISEA J204611.70-575550.0
J203826.6-561509	309.611	-56.253	0.368	28.870	185	3.910	1.701	741	0.006	J203825.76-561522.3
J205146.0-604621	312.942	-60.773	0.337	3.043	89	25.940	6.387	1165	0.037	J205145.73-604623.1
J204408.5-603931	311.035	-60.659	0.121	2.018	42	3.832	1.882	838	0.003	2MASX J20441046-6039212
J204008.3-503254	310.035	-50.549	0.149	54.060	121	7.783	3.020	972	0.074	2MASX J20401004-5032544
J205555.5-545538	313.981	-54.927	0.140	21.865	187	14.443	4.660	1127	0.120	2MASX J20555594-5455493
J205156.7-523751	312.987	-52.631	0.045	4.952	16	1.838	1.166	732	0.018	ESO 187-26
J204822.8-613113	312.095	-61.520	0.108	0.750	126	7.862	3.086	993	0.006	2MASX J20482154-6131025
J205316.0-620912	313.317	-62.154	0.395	0.313	109	13.545	3.978	973	0.011	J205315.09-620906.2
J210114.4-554134	315.310	-55.693	0.260	0.750	75	19.559	5.486	1140	0.002	LEDA 406911
J205943.1-501908	314.930	-50.319	0.331	0.763	84	7.361	2.659	872	0.002	J205941.29-501810.3
J211652.8-593039	319.220	-59.511	0.058	60.742	32	4.347	2.089	886	0.018	FRL 95
J210604.1-584425	316.517	-58.740	1.126	8.465	382	202.092	17.422	1195	0.014	[FAB2011] 316.50647-58.73848
J211250.8-531753	318.212	-53.298	0.223	8.623	65	9.300	3.328	978	0.062	LEDA 431554
J212023.5-542845	320.098	-54.479	0.241	5.831	149	7.038	2.720	909	0.016	J212025.34-542840.9
J210732.3-552840	316.885	-55.478	0.349	2.027	128	12.747	3.898	984	0.016	J210732.69-552821.0
J211144.8-533856	317.937	-53.649	0.443	3.612	113	15.140	4.190	972	0.011	J211144.61-533852.8
J212251.3-582948	320.714	-58.497	0.293	0.750	82	10.150	3.425	962	0.015	WISEA J212249.41-582941.9
J213151.8-500345	322.966	-50.063	0.457	0.750	209	21.909	5.376	1051	0.018	J213151.23-500344.2
J213003.2-504832	322.514	-50.809	0.076	46.760	40	6.662	2.794	970	0.001	2MASX J21294244-5049260
J212809.3-484330	322.039	-48.725	0.321	0.750	142	5.134	2.101	809	0.009	J212809.39-484346.8
J213800.9-600758	324.504	-60.133	0.319	5.875	85	54.931	10.906	1402	0.003	[RBB2014] J213800.82-600753.8
J212433.5-612500	321.140	-61.417	0.436	17.086	127	34.158	7.389	1177	0.006	[RBB2014] J212434.77-612444.4
J213305.7-594531	323.274	-59.759	0.505	0.258	252	22.120	5.268	1024	0.007	J213305.59-594537.1
J213221.5-585412	323.090	-58.903	0.496	2.215	129	15.786	4.192	952	0.022	J213221.89-585414.1
J214528.9-513623	326.371	-51.606	0.054	0.750	18	1.333	0.937	679	0.318	2MASX J21452953-5136250
J213505.3-625454	323.772	-62.915	0.223	4.264	103	5.903	2.482	887	0.005	LEDA 338113
J214359.4-563717	325.998	-56.622	0.082	168.404	48	12.907	4.377	1125	0.570	MRC 2140-568
J214622.3-571714	326.593	-57.287	0.073	4.689	41	9.799	3.631	1060	0.243	FAIRALL 0116
J214553.0-564448	326.471	-56.747	0.481	2.758	182	51.416	9.632	1264	0.007	[RBB2014] J214551.96-564453.5
J213536.8-572622	323.903	-57.440	0.427	4.632	216	28.547	6.568	1136	0.008	[RBB2014] J213537.41-572630.7
J214647.5-573648	326.698	-57.614	0.611	1.018	164	33.250	6.585	1058	0.035	[BRS2016] J214648.41-573653.7
J214758.4-572019	326.993	-57.339	0.142	0.750	107	5.916	2.521	917	0.002	0
J215813.2-485044	329.555	-48.846	0.499	0.750	109	7.569	2.499	800	0.014	J215812.61-485031.7
J215129.7-552019	327.874	-55.339	0.041	2623.450	80	1.761	1.150	730	0.074	2MASX J21512991-5520124
J220153.8-595644	330.474	-59.946	0.107	2.129	48	47.838	10.776	1507	0.038	ESO 146-5
J220504.4-592716	331.268	-59.455	0.350	2.647	154	22.796	5.845	1126	0.010	J220500.42-592716.9
J215444.0-593638	328.684	-59.611	0.429	2.036	147	23.542	5.736	1085	0.003	J215446.49-593634.0
J214844.5-611650	327.185	-61.281	0.572	2.545	158	37.403	7.294	1111	0.003	[RBB2014] J214838.82-611555.9
J215826.3-602359	329.610	-60.400	0.085	17.604	54	5.648	2.494	932	0.005	2MASX J21582577-6023286
J220052.4-515502	330.219	-51.917	0.218	6.362	112	10.970	3.746	1019	0.011	LEDA 451041
J215625.0-513110	329.105	-51.520	0.494	1.940	116	24.325	5.657	1053	0.034	J215624.79-513119.4
J220756.6-522333	331.986	-52.393	0.111	2.340	40	3.082	1.619	800	0.010	J220757.72-522320.2
J215815.7-502328	329.566	-50.391	0.488	0.750	106	25.476	5.886	1069	0.010	J215817.77-502352.7
J220604.7-494313	331.520	-49.720	0.128	5.430	62	1.284	0.883	650	0.018	2MASX J22060802-4943077
J215919.0-521025	329.829	-52.174	0.498	3.824	151	17.470	4.498	974	0.005	J215919.21-520953.1

Table A.1. continued.

Cluster ID	RA	DEC	z	S_{Radio} (mJy)	LLS (kpc)	L_X (10^{43} erg s^{-1})	M ($10^{14} M_\odot$)	r_{500}	n_e (cm^{-3})	BCG ID
J215515.7-514004	328.815	-51.668	0.228	0.750	65	1.404	0.903	632	0.659	2dFGRS TGS823Z290
J215406.4-575136	328.527	-57.860	0.075	1.363	29	22.077	6.373	1278	0.005	2MASX J21540421-5752033
J215918.0-564510	329.825	-56.753	0.279	0.750	76	15.875	4.684	1074	0.335	WISEA J215918.14-564459.1
J221033.1-570945	332.638	-57.163	0.300	0.925	83	11.120	3.636	979	0.005	2dFGRS TGS812Z361
J220952.8-553521	332.470	-55.589	0.168	135.047	137	3.865	1.858	821	0.008	LEDA 407921
J221117.3-483401	332.822	-48.567	0.257	1.026	96	27.300	6.899	1232	0.004	LEDA 486024
J220731.3-492529	331.881	-49.425	0.254	13.086	101	5.273	2.238	847	0.006	J220733.00-492444.0
J220112.5-614737	330.302	-61.794	0.238	10.265	85	13.025	4.166	1048	0.126	LEDA 352331
J221631.8-532501	334.133	-53.417	0.180	83.864	80	4.536	2.064	847	0.008	LEDA 430211
J221454.0-532017	333.725	-53.338	0.338	144.263	210	5.068	2.072	800	0.007	J221454.87-532100.6
J220920.7-514811	332.336	-51.803	0.117	0.791	40	12.732	4.321	1107	0.001	LEDA 163750
J222327.0-522740	335.863	-52.461	0.273	22.105	194	12.071	3.891	1012	0.008	WISEA J222321.82-522749.3
J222000.0-522730	335.000	-52.459	0.106	0.439	32	7.729	3.055	990	0.000	2MASX J22200853-5227489
J222120.9-501707	335.337	-50.286	0.179	600.143	129	5.556	2.376	888	0.010	LEDA 468032
J221504.0-520501	333.767	-52.084	0.500	2.117	148	26.143	5.939	1068	0.003	LEDA 448827
J222420.5-503901	336.085	-50.650	0.335	0.750	153	8.557	3.018	908	0.008	J222417.04-503859.3
J221959.2-482901	334.997	-48.484	0.871	0.750	131	81.107	10.560	1116	0.008	0
J222251.8-483423	335.716	-48.573	0.652	0.476	119	68.961	11.090	1238	0.007	[BRS2016] J222250.73-483435.5
J221959.1-581546	334.996	-58.263	0.281	6.828	90	7.639	2.826	907	0.002	J221958.01-581620.9